Exceptionally large winding number of a finite-size topological superconductor

Satoshi Ikegaya [1,2,3] Shingo Kobayashi [4] and Yasuhiro Asano [3]
[1]*Institute for Advanced Research, Nagoya University, Nagoya 464-8601, Japan*
[2]*Department of Applied Physics, Nagoya University, Nagoya 464-8603, Japan*
[3]*Department of Applied Physics, Hokkaido University, Sapporo 060-8628, Japan*
[4]*RIKEN Center for Emergent Matter Science, Wako, Saitama 351-0198, Japan*

(Received 8 April 2025; revised 9 December 2025; accepted 28 January 2026; published 23 February 2026)

We study finite-size-induced topological phenomena in unconventional superconductors. Specifically, we focus on a thin film with a persistent spin texture, fabricated on a high-T_c cuprate d_{xy}-wave superconductors. In two-dimensional d_{xy}-wave superconductors, flat-band Andreev bound states appear at the edges. As the system narrows, these bound states acquire an energy gap due to finite-size hybridization and spin-orbit coupling of the persistent spin texture. This induced gap gives rise to the emergence of a topological phase, characterized by an exceptionally large one-dimensional winding number that scales with the film width. We demonstrate the appearance of highly degenerate zero-energy states, leading to anomalous perfect charge transport in dirty superconducting junctions.

DOI: 10.1103/rf8j-lf4s

I. INTRODUCTION AND OUTLINE

Topological phases of matter, characterized by nontrivial topological invariants associated with gapped band structures, have been a central focus of condensed matter physics. A hallmark of these phases, as dictated by the bulk-boundary correspondence, is the emergence of exotic boundary states. The intrinsic stability of these states holds promise for future applications in quantum technologies [1–5]. The topological invariant of gapped band structures is determined primarily by two factors: the dimensionality and the symmetry of the systems [6]. The relationship between topological properties and dimensionality is of particular importance in quasi-$(d-1)$-dimensional systems, where the size of a d-dimensional system is reduced along one direction. In such systems, topological properties can undergo marked changes as the system approaches the dimensional crossover regime [7,8].

A representative example is found in quasi-two-dimensional thin films of topological insulators. In three-dimensional topological insulators, Dirac surface states appear as a consequence of a $\mathbb{Z}_2$ topological invariant. In quasi-two-dimensional systems, finite-size effects induce hybridization between the Dirac surface states on the top and bottom surfaces, leading to two-dimensional (2D) topological insulators [7,9–11], depending on the parity of the number of stacked 2D layers [12,13]. These coupled Dirac surface states can be further engineered by additional perturbations. For instance, applying an exchange potential opens a gap in the Dirac spectrum and stabilizes a topological phase characterized by the Chern number [14], while an extended s-wave pairing potential can induce a $\mathbb{Z}_2$ topological superconducting phase [15,16].

Despite the extensive study of topological phases originating from Dirac surface states [14,16–28], topological phases driven by Andreev bound states (ABSs) of superconductors (SCs) remain poorly understood. A known case involves topological phases originating from gapped Caroli–de Gennes–Matricon bound states in vortex cores [29–39], which result from the phase winding around a vortex rather than a finite-size effect. Although topological superconducting phases under finite-size effects have been studied [8,40,41], they do not concern the energy gaps of surface ABSs. Therefore, superconducting analogs of topological phases induced by finite-size effects remain largely unexplored.

The main purpose of this paper is to uncover finite-size-induced topological phenomena of superconducting systems. We consider a thin film exhibiting a persistent spin texture (PST) [42–55], fabricated on a high-T_c cuprate d_{xy}-wave SC [see Fig. 1(a)]. Specifically, we assume that a unidirectional spin-orbit coupling (SOC), which is responsible for the formation of the PST [42–55], and a proximity-induced d_{xy}-wave pair potential coexist in the thin film. A 2D d_{xy}-wave SC is a prototypical nodal topological SC, hosting flat-band ABSs at its edges [56–60] [see Fig. 1(b)]. Reducing the system size in one direction induces finite-size effects, resulting in a characteristic energy dispersion in the ABS spectrum, where multiple band crossings occur at zero energy [see Fig. 1(c)]. Furthermore, introducing the unidirectional SOC of the PST opens a full energy gap in the ABS spectrum [see Fig. 1(d)]. The resulting gapped quasi-one-dimensional (Q1D) system falls into the chiral symmetry class (class AIII) of the Altland-Zirnbauer (AZ) classification [6]. This class allows a $\mathbb{Z}$ topological invariant in one dimension, namely, a one-dimensional (1D) winding number. This winding number can take unusually large values, which almost coincides with the number of the propagating channels in the Q1D system [see Fig. 2(a)]. The appearance of highly degenerate zero-energy edge states (ZESs), associated with this exceptionally large winding number, is confirmed [see Fig. 2(b)]. We demonstrate that these ZESs lead to prominent zero-bias conductance quantization in *dirty* normal-metal–SC (NM–SC)

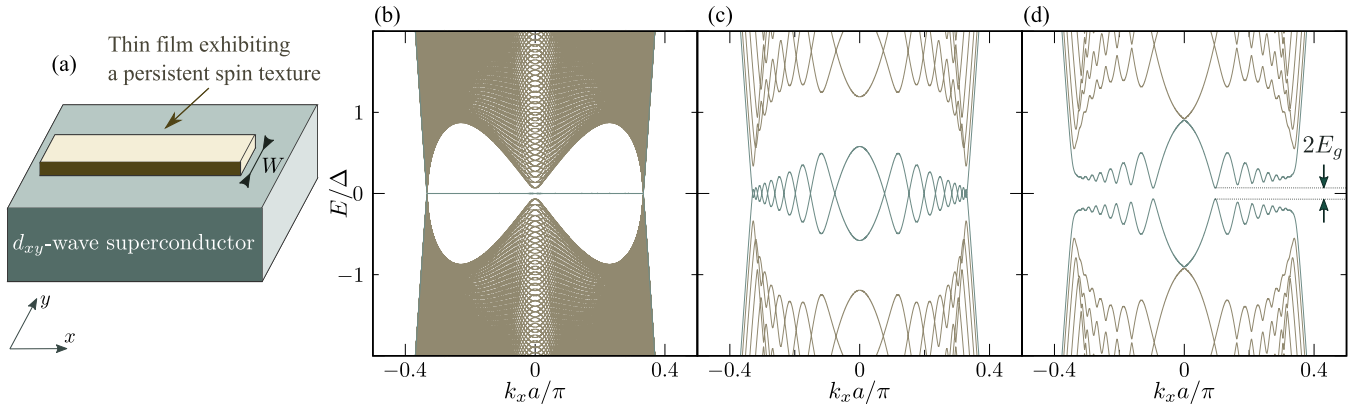

FIG. 1. (a) Schematic of the system under consideration, where the unidirectional SOC potential of the PST and the proximity-induced d_{xy}-wave pair potential coexist in the thin film. [(b)–(d)] Energy spectra as a function of k_x for (b) $(W, \lambda) = (800a, 0)$, (c) $(W, \lambda) = (30a, 0)$, and (d) $(W, \lambda) = (30a, 0.5t)$, with an open boundary condition applied in the y direction. As shown in (d), the energy spectrum of the ABS exhibits a gap, E_g, resulting from the finite-size hybridization and unidirectional SOC.

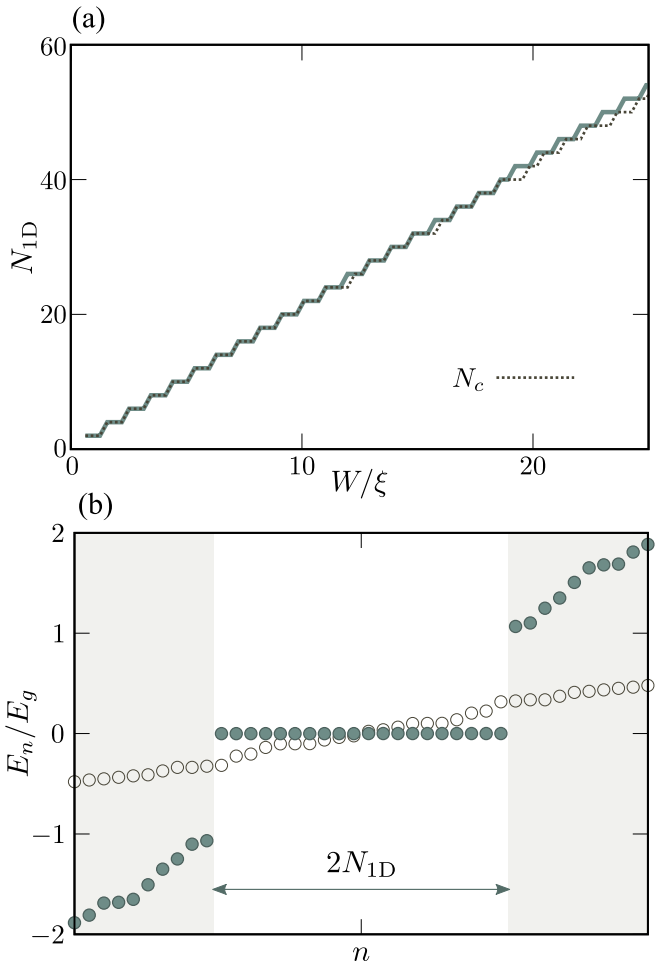

FIG. 2. (a) 1D winding number, N_{1D}, as a function W, with dotted line representing the number of the propagating channels N_c. (b) Energy spectrum under open boundary conditions in both x and y directions, where the colored (white) dots indicate the result for $\lambda = 0.5t$ ($\lambda = 0$). Each dot corresponds to twofold-degenerate states due to Kramars degeneracy. For $\lambda = 0.5t$, we clearly observe the emergence of N_{1D}-fold-degenerate ZESs.

junctions (see Fig. 5). This disorder-independent perfect charge transport is analogous to the anomalous proximity effects of 2D spin-triplet p_x-wave SCs that host flat-band Majorana bound states [61–71].

High-T_c cuprates are employed as the parent SC due to their large superconducting gap [72,73], which implies that the induced energy gap in ABSs will be sufficiently large for experimental observation. The PST was originally discovered in zinc-blende semiconductor quantum wells [43,44]. More recently, the formation of the PST has been predicted in a variety of 2D materials, including wurtzite-structured semiconductors [45], ferroelectric semiconductors [46–52], monolayer transition-metal dichalcogenides [53,54], and group IV-V compounds [55], enabling the experimental realization of the proposed system. Consequently, we propose an intriguing route for exploring novel topological superconducting phases driven by gapped ABSs.

II. EMERGENCE OF ZERO-ENERGY STATES

We describe the present system using a 2D tight-binding model on a square lattice. A lattice site is indicated by a vector $\boldsymbol{r} = j\boldsymbol{x} + m\boldsymbol{y}$, where $|\boldsymbol{x}| = |\boldsymbol{y}| = a$. We apply a periodic boundary condition in the x direction, while an open boundary condition is applied in the y direction; the thin film is placed on $1 \leqslant m \leqslant M$, with $W = Ma$ representing the width of the system. The Bogoliubov–de Gennes (BdG) Hamiltonian reads

$$
\begin{aligned}
H &= \frac{1}{2}\sum_{k_x} C_{k_x}^{\dagger} H_{k_x} C_{k_x}, \\
C_{k_x}^{\dagger} &= \left[c_{k_x,\uparrow}^{\dagger}, c_{k_x,\downarrow}^{\dagger}, c_{-k_x,\uparrow}^{\mathrm{T}}, c_{-k_x,\downarrow}^{\mathrm{T}}\right], \\
c_{k_x,s} &= \left[c_{k_x,1,s}, c_{k_x,2,s}, \cdots, c_{k_x,M,s}\right]^{\mathrm{T}}, \\
H_{k_x} &= \xi_{k_x} \otimes \tau_z + \Lambda \otimes s_z - \Delta_{k_x} \otimes s_y \otimes \tau_y, \\
\xi_{k_x} &= -2t\cos(k_x a) - \mu + 4t - tA_+, \\
\Lambda &= \frac{i\lambda}{2} A_-, \quad \Delta_{k_x} = \frac{i\Delta}{2}\sin(k_x a) A_-,
\end{aligned}
\tag{1}
$$

where $A_\pm$ is the $(M \times M)$ matrices with

$$(A_\pm)_{ij} = \begin{cases} 1 & \text{for } i = j+1 \\ \pm 1 & \text{for } i = j-1, \\ 0 & \text{otherwise} \end{cases} \tag{2}$$

$c_{k_x,m,s}$ is an annihilation operator of an electron at $y = ma$ with momentum k_x and spin s $(=\uparrow, \downarrow)$, t denotes the nearest-neighbor hopping integral, μ is the chemical potential, λ represents the strength of the unidirectional SOC forming the PST, and Δ denotes the proximity-induced spin-singlet d_{xy}-wave pair potential [74–80]. τ_ν and s_ν for $\nu = x, y, z$ denote the Pauli matrices in Nambu and spin spaces, respectively. When we apply a periodic boundary condition in both x and y directions, the BdG Hamiltonian is rewritten as $H_{\boldsymbol{k}} = \xi_{\boldsymbol{k}}\tau_z + \lambda \sin(k_y a) s_z - \Delta_{\boldsymbol{k}} s_y \otimes \tau_y$, with $\xi_{\boldsymbol{k}} = -2t\cos(k_x a) - 2t\cos(k_y a) - \mu + 4t$ and $\Delta_{\boldsymbol{k}} = \Delta \sin(k_x a)\sin(k_y a)$. The PST inherently guarantees spin-rotational symmetry [43,44]:

$$\left[R_z, H_{k_x}\right] = 0, \quad R_z = i s_z \otimes \tau_z, \tag{3}$$

where R_z describes the spin rotation along the z axis. Therefore, we can decompose the Hamiltonian into two subsectors, each corresponding to a different eigenvalue of R_z:

$$\begin{aligned} H &= \frac{1}{2}\sum_{k_x,s} C^\dagger_{k_x,s} H_{k_x,s} C_{k_x,s}, \\ C^\dagger_{k_x,s} &= \left[c^\dagger_{k_x,s}, c^{\mathrm{T}}_{-k_x,\bar{s}}\right], \\ H_{k_x,s} &= \begin{bmatrix} \xi_{k_x} + \sigma_s \Lambda & \sigma_s \Delta_{k_x} \\ \sigma_s \Delta_{k_x} & -\xi_{k_x} - \sigma_s \Lambda \end{bmatrix}, \end{aligned} \tag{4}$$

where $\bar{s}$ represents the opposite spin of s, and $\sigma_s = +1(-1)$ for $s =\uparrow (\downarrow)$. In the *absence* of the SOC (i.e., $\lambda = 0$), the block component $H_{k_x,s}$ belongs to class CI of the AZ classification:

$$\begin{aligned} T H_{k_x,s} T^{-1} &= H_{-k_x,s}, \quad T = \mathcal{K}, \\ C H_{k_x,s} C^{-1} &= -H_{-k_x,s}, \quad C = \tau_y \mathcal{K}, \\ \Gamma H_{k_x,s} \Gamma^{-1} &= -H_{k_x,s}, \quad \Gamma = \tau_y, \end{aligned} \tag{5}$$

where $\mathcal{K}$ denotes the complex conjugation operator, and the symmetry operators satisfy $T^2 = 1$, $C^2 = -1$, and $\Gamma^2 = 1$. However, in the *presence* of the SOC (i.e., $\lambda \neq 0$), the block component $H_{k_x,s}$ falls into class AIII, preserving only the chiral symmetry Γ. According to the AZ classification [6], a *fully gapped* energy spectrum of $H_{k_x,s}$ allows us to define the 1D winding number:

$$N_{1\mathrm{D}} = \frac{i}{4\pi}\sum_{s=\uparrow,\downarrow}\int dk_x \mathrm{Tr}\left[\Gamma H^{-1}_{k_x,s}\partial_{k_x} H_{k_x,s}\right] \in \mathbb{Z}, \tag{6}$$

where the trace is taken over both the Nambu space and the lattice sites along the y direction. The unidirectional SOC is essential for defining the 1D winding number $N_{1\mathrm{D}}$, as generic SOCs such as Rashba SOC break spin-rotation symmetry. In this case, the Q1D systems are in class DIII, and the AZ classification changes from $\mathbb{Z}$ to $\mathbb{Z}_2$.

Figures 1(b)–1(d) present the energy eigenvalues of $H_{k_x,s}$ as a function of k_x, which are obtained by diagonalizing $H_{k_x,s}$ numerically. The parameters are set as $\mu = t$ and $\Delta = 0.2t$. The superconducting coherence length is evaluated as $\xi = 1/\{\pi \mathrm{artanh}(\Delta/2t)\} \sim 3.17a$. Note that the energy eigenvalues of $H_{k_x,\uparrow}$ and those of $H_{k_x,\downarrow}$ are completely overlapped due to Kramers degeneracy. In Fig. 1(b) we plot the energy eigenvalues with $\lambda = 0$, where the system width is sufficiently larger than the superconducting coherence length, $W = 800a \sim 252\xi$. In this regime, the flat-band ABSs are clearly visible at zero energy. In Fig. 1(c) we show the energy eigenvalues with $\lambda = 0$ in a narrower system with $W = 30a \sim 9.46\xi$. The finite-size effects lead to hybridization between the ABSs localized at $y/a = 1$ and $y/a = W/a$, resulting in the breakdown of the flat-band structure. Nevertheless, multiple band crossings persist at zero energy. As detailed in Appendix A, these band crossings are protected by inversion symmetry [81,82], which holds only in the absence of the SOC (i.e., $\lambda = 0$). Consequently, introducing the unidirectional SOC is expected to open a full energy gap in the ABS spectrum. This is indeed observed in Fig. 1(d), where the SOC is introduced with $\lambda = 0.5t$. Since $H_{k_x,s}$ now describes the gapped systems in class AIII, the 1D winding number $N_{1\mathrm{D}}$ in Eq. (6) becomes well defined.

In Fig. 2(a) the 1D winding number $N_{1\mathrm{D}}$ is plotted as a function of the system width W, with $\lambda = 0.5t$. The results show that $N_{1\mathrm{D}}$ increases with W and reaches values substantially larger than unity. For instance, at $W = 30a \sim 9.46\xi$, the winding number reaches $N_{1\mathrm{D}} = 20$. The dotted line denotes the number of the propagating channels $N_c = 2n_c$, where n_c is the largest integer satisfying $\mu > 2t\{1 - \cos(\frac{n_c\pi}{W+1})\}$. The factor of 2 reflects spin degeneracy. Notably, $N_{1\mathrm{D}}$ closely tracks N_c, and the underlying mechanism is discussed later. The bulk-boundary correspondence guarantees the presence of $N_{1\mathrm{D}}$-fold-degenerate ZESs at the system edge. In Fig. 2(b) we show the energy eigenvalues under open boundary conditions in both x and y directions, where the system is placed on $1 \leqslant j \leqslant L/a$. We choose $W = 30a \sim 9.46\xi$ and $L = 600a \sim 189.27\xi$. The colored (white) dots indicate the result for $\lambda = 0.5t$ $(\lambda = 0)$; each dot represents a twofold-degenerate state caused by Kramers degeneracy. In the absence of SOC, the energy spectrum remains gapless. When SOC is present, $2N_{1\mathrm{D}}$ ZESs appear inside the finite energy gap E_g, where the factor of 2 arises from both edges in the x direction. Under the present parameters, the system hosts 40 ZESs. The winding number is limited by the number of Fermi points in the 1D Brillouin zone [60], which typically results in small values. In contrast, the proposed Q1D system exhibits multiple band crossings due to the finite-size effect and consequently supports an exceptionally large number of the topologically protected ZESs. The winding number remains well defined as long as the system preserves the chiral symmetry given by Eq. (5). Consequently, the ZESs retain their high degree of degeneracy even in the presence of perturbations that respect this symmetry, such as nonmagnetic disorder.

We examine the size of the induced energy gap, E_g, as also indicated in Fig. 1(d). In Fig. 3 E_g is plotted as a function of the system width W. The solid and dashed lines correspond to $\lambda = 0.5t$ and $\lambda = t$, respectively. As W increases, the induced gap E_g exhibits oscillatory decay, with larger values of λ yielding larger gaps. We now adopt $Bi_2Sr_2CaCu_2O_8$ as the parent SC, which has a large superconducting gap, $\Delta \sim 30$ meV [72,73]. With its in-plane lattice constant $a \sim 5.4$ Å, the superconducting coherent length is estimated as $\xi \sim 1.71$ nm.

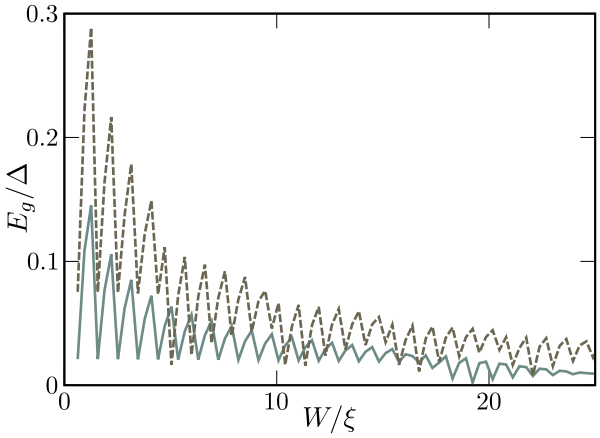

FIG. 3. Induced energy gap, E_g, as a function of the system width, W, where the solid (dashed) line shows the result for $\lambda = 0.5t$ ($\lambda = t$).

As an example, when $W = 64a \sim 20.21\xi \sim 34.6$ nm and $\lambda a = ta = 5\Delta a \sim 810$ meVÅ, the resulting induced gap is $E_g = 0.044\Delta \sim 1.3$ meV, which remains sufficiently large for experimental observation. Moreover, compatible or even stronger SOCs, reaching several eV Å, have been theoretically predicted in various 2D systems with a PST (see, for example, Refs. [54,55]). Thus, while a more microscopic evaluation of E_g remains as an crucial future task, these results suggest that topological phases protected by the induced gap of ABSs could be experimentally accessible.

III. EFFECTIVE THEORY

To obtain an intuitive understanding of the numerical results, we derive a low-energy effective Hamiltonian. For this purpose we consider the BdG equation in the continuum limit:

$$H_s(k_x, y)\psi_s(k_x, y) = E\psi_s(k_x, y), \tag{7}$$

with

$$\begin{aligned}
H_s(k_x, y) &= H_s^{d_{xy}}(k_x, y) + H_s^{\lambda}(y),\\
H_s^{d_{xy}}(k_x, y) &= \begin{bmatrix} \xi(k_x, y) & \sigma_s\Delta(k_x, y) \\ \sigma_s\Delta(k_x, y) & -\xi(k_x, y) \end{bmatrix},\\
H_s^{\lambda}(y) &= \sigma_s \begin{bmatrix} \Lambda(y) & 0 \\ 0 & -\Lambda(y) \end{bmatrix},\\
\xi(k_x, y) &= -\frac{\hbar^2}{2m}\partial_y^2 - \tilde{\mu}, \quad \tilde{\mu} = \mu - \frac{\hbar^2 k_x^2}{2m},\\
\Delta(k_x, y) &= -i\frac{\tilde{\Delta}}{k_F}\partial_y, \quad \tilde{\Delta} = \frac{\Delta k_x}{k_F}, \quad \Lambda(y) = -i\tilde{\lambda}\partial_y,
\end{aligned} \tag{8}$$

where $ta^2 = \hbar^2/(2m)$, $\lambda a = \tilde{\lambda}$, and $k_F = \sqrt{2m\mu}/\hbar$ denotes the Fermi wave number. We first explore the wave functions of the ABSs in the absence of the SOC, satisfying

$$H_s^{d_{xy}}(k_x, y)\psi_s^{\pm}(k_x, y) = \pm\epsilon_s(k_x)\psi_s^{\pm}(k_x, y), \tag{9}$$

where $\pm\epsilon_s(k_x)$ represents the energy eigenvalues of the ABSs, as also illustrated in Fig. 4(a). While obtaining $\epsilon_s(k_x)$ and $\psi_s^{\pm}(k_x, y)$ across the entire range of k_x is challenging, as detailed in Appendix B, we can analytically solve the BdG

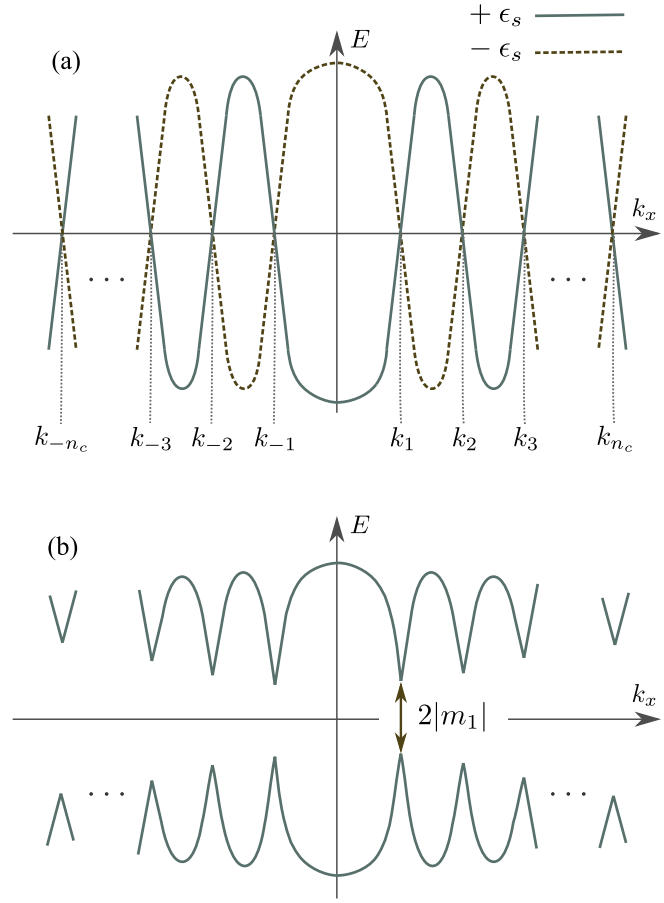

FIG. 4. Schematic of the energy spectra of the ABSs for (a) $\tilde{\lambda} = 0$ and for (b) $\tilde{\lambda} \neq 0$, described by the effective Hamiltonian in Eq. (13).

equation at momenta where zero-energy band crossings occur: $H_s^{d_{xy}}(k_n, y)\psi_s^{\pm}(k_n, y) = 0$. Specifically, the zero-energy band crossings occur at momenta

$$\begin{aligned}
k_n &= \mathrm{sgn}[n]\sqrt{\frac{k_F^2 - q_n^2}{1 + \left(\frac{\Delta}{2\mu}\right)^2}},\\
n &= \pm 1, \pm 2, \ldots, \pm n_c,
\end{aligned} \tag{10}$$

with the corresponding zero-energy wave functions

$$\begin{aligned}
\psi_s^{\pm}(k_n, y) &= \begin{cases} e^{\mp i\frac{\pi}{4}}\varphi_s^{\pm}(k_n, y) & \text{for } |n| \in \text{odd} \\ e^{\mp i\frac{\pi}{4}}\varphi_s^{\mp}(k_n, y) & \text{for } |n| \in \text{even} \end{cases},\\
\varphi_s^{\pm}(k_n, y) &= \frac{1}{2}\begin{bmatrix} \phi_{s,+}(k_n, y) \pm \phi_{s,-}(k_n, y) \\ i\{\phi_{s,+}(k_n, y) \mp \phi_{s,-}(k_n, y)\} \end{bmatrix},\\
\phi_{s,\pm}(k_n, y) &= c_{k_n,s,\pm}\sin(q_n y)e^{\pm\sigma_s\kappa_n y},\\
q_n &= \frac{n\pi}{W}, \quad \kappa_n = \frac{\Delta}{2\mu}k_n, \quad c_{k_n,s,\pm} = \sqrt{\frac{2X_n}{W}e^{\mp\sigma_s\kappa_n W}}\\
X_n &= \frac{\kappa_n W}{\sinh(\kappa_n W)}\left\{1 + \left(\frac{\Delta}{2\mu}\right)^2\frac{k_n^2}{q_n^2}\right\},
\end{aligned} \tag{11}$$

where n_c in the continuum limit is given by $n_c = [Wk_F/\pi]_G$, with $[\cdots]_G$ representing the Gauss symbol, which takes the integer part of the argument. A detailed derivation for Eq. (11) is provided in Appendix B. Notably, the total number of zero-energy band crossings coincides with the number of propagating channels, $N_c = 2n_c$ [see Fig. 4(a)]. To proceed with our analysis, we treat the SOC, $H_s^{\lambda}(y)$, as a perturbation and construct the low-energy effective Hamiltonian as follows:

$$H_s^{\rm eff}(k_x) = \begin{bmatrix} A_{++} & A_{+-} \\ A_{-+} & A_{--} \end{bmatrix} + O(\lambda^2),$$
$$A_{\eta\eta'} = \int dy \{\psi_s^{\eta}(k_x, y)\}^{\dagger} H_s(k_x, y) \psi_s^{\eta'}(k_x, y), \tag{12}$$

where $A_{\eta\eta} = \eta\epsilon_s(k_x)$. In the vicinity of $k_x = k_n$, we obtain, $H_s^{\rm eff}(k_n + \delta k) = H_{n,s}^{\rm eff}(\delta k) + O(\delta k^2)$, with

$$H_{n,s}^{\rm eff}(\delta k) = \begin{cases} \begin{bmatrix} v_n \delta k & m_n \\ m_n & -v_n \delta k \end{bmatrix} & \text{for } |n| \in \text{odd} \\ \begin{bmatrix} -v_n \delta k & -m_n \\ -m_n & v_n \delta k \end{bmatrix} & \text{for } |n| \in \text{even} \end{cases},$$
$$v_n = \frac{\hbar^2 k_n}{m} \left\{ 1 + \left(\frac{\Delta}{2\mu} \right)^2 \right\} X_n, \quad m_n = \tilde{\lambda} \kappa_n X_n, \tag{13}$$

where m_n represents the mass term that opens the energy gap in the ABS spectrum, as depicted in Fig. 4(b). A detailed derivation for Eq. (13) is provided in Appendix B. The low-energy effective Hamiltonian preserves chiral symmetry:

$$\gamma H_s^{\rm eff}(k_x) \gamma^{-1} = -H_s^{\rm eff}(k_x), \quad \gamma = \begin{bmatrix} 0 & -i \\ i & 0 \end{bmatrix}, \tag{14}$$

which allows us to define the winding number:

$$N_{\rm 1D}^{\rm eff} = \frac{i}{4\pi} \sum_s \int dk_x \mathrm{Tr} \left[\gamma \left\{ H_s^{\rm eff}(k_x) \right\}^{-1} \partial_{k_x} H_s^{\rm eff}(k_x) \right]. \tag{15}$$

On the basis of Ref. [60], we can compute $N_{\rm 1D}^{\rm eff}$ using only the Hamiltonian in the vicinity of $k_x = k_n$:

$$N_{\rm 1D}^{\rm eff} = \frac{1}{2} \sum_s \sum_{n=-n_c}^{n_c} \mathrm{sgn}[v_n] \mathrm{sgn}[m_n], \tag{16}$$

where the detailed derivation of Eq. (16) is provided in Appendix C. Applying this formula, we eventually obtain

$$N_{\rm 1D}^{\rm eff} = N_c, \tag{17}$$

which shows excellent agreement with the numerical result shown in Fig. 2(a). Consequently, our effective theory confirms that the nontrivial topology of the present systems indeed originates from the energy gap of the ABSs.

IV. ANOMALOUS PROXIMITY EFFECT

Finally, we describe anomalous charge transport induced by the $N_{\rm 1D}$-fold-degenerate ZESs. We consider a junction consisting of three segments: a ballistic NM segment for $-\infty \leqslant j < 1$, a dirty NM segment for $1 \leqslant j \leqslant L_D/a$, and a SC segment for $L_D/a < j \leqslant \infty$. For numerical calculations, the BdG Hamiltonian in Eq. (1) is reformulated in a real-space basis by performing a Fourier transformation along the x direction: $c_{k_x,m,s} \to c_{r,s}$. The proximity-induced pair potential is assumed to exist only in the SC segment, i.e., $j > L_D/a$. For the dirty NM segment, we introduce a nonmagnetic random on-site potential:

$$H_D = \sum_{j=1}^{L_D/a} \sum_{m,s} v_{\boldsymbol{r}} c_{\boldsymbol{r},s}^{\dagger} c_{\boldsymbol{r},s}, \tag{18}$$

where $v_{\boldsymbol{r}}$ is given randomly in the range $-v_{\rm imp}/2 \leqslant v_{\boldsymbol{r}} \leqslant v_{\rm imp}/2$. We calculate the differential conductance at zero temperature on the basis of the Blonder–Tinkham–Klapwijk formalism [83]:

$$G(eV) = \frac{e^2}{h} \sum_{\zeta,\eta} \left[\delta_{\zeta,\eta} - \left| r_{\zeta,\eta}^{ee} \right|^2 + \left| r_{\zeta,\eta}^{he} \right|^2 \right]_{E=eV}, \tag{19}$$

where $r_{\zeta,\eta}^{ee}$ and $r_{\zeta,\eta}^{he}$ denote a normal and an Andreev reflection coefficient at energy E, respectively. The indices ζ and η correspond to the outgoing and incoming channels. These reflection coefficients are calculated using recursive Green's function techniques [84,85]. For numerical calculations, the parameters are fixed as $\mu = t$, $\Delta = 0.2t$, $v_{\rm imp} = 0.5t$, and $W = 30a$. The conductance is averaged over 5×10^3 samples with different random potential configurations.

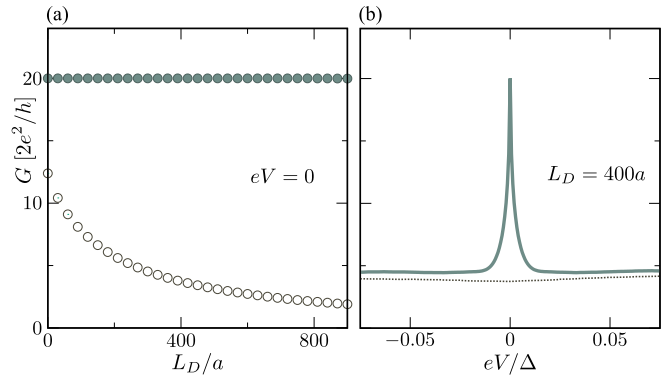

FIG. 5. (a) Zero-bias conductance as a function of the length of the dirty NM segment, L_D, with the colored (white) dots representing the result for $\lambda = 0.5t$ ($\lambda = 0$). (b) Conductance spectra at $L_D = 400a$, with the solid (dashed) line representing the result for $\lambda = 0.5t$ ($\lambda = 0$). For the finite-size-induced topological phase (i.e., $\lambda = 0.5t$), we observe zero-bias conductance quantization at $(2e^2/h)N_{\rm 1D}$, independent of L_D.

In Fig. 5(a) we plot the differential conductance at zero bias as a function of the length of the dirty NM segment. The colored (white) dots correspond to $\lambda = 0.5t$ ($\lambda = 0$). In the absence of SOC, the zero-bias conductance decreases monotonically with increasing L_D. In contrast, for $\lambda = 0.5t$, the zero-bias conductance remains perfectly quantized, independent of L_D:

$$G(0) = \frac{2e^2}{h} \times N_{\rm 1D} = \frac{2e^2}{h} \times N_c, \tag{20}$$

where $N_{\rm 1D} = 20$ for the given parameters. Moreover, the conductance spectrum for $\lambda = 0.5t$ exhibits a prominent zero-bias peak, as shown in Fig. 5(b). This perfect conductance quantization suggests that the $N_{\rm 1D}$-fold-degenerate ZESs,

initially localized at the junction interface, penetrate into the dirty NM segment while retaining their high degree of degeneracy. Therefore they form perfect transmission channels within the dirty NM-SC junction [64,65]. This unusual superconducting proximity effect, accompanied by the penetration of topologically protected ZESs, is analogous to the anomalous proximity effect observed in 2D nodal p_x-wave SCs [61,62]. As a result, we propose a striking perfect charge transport that clearly manifests the presence of highly degenerate ZESs.

V. DISCUSSION

In Appendix D we also confirm that highly degenerate ZESs can appear in the bilayer Hamiltonian, where the first and second layers describe a nonsuperconducting quasi-one-dimensional thin film with unidirectional spin–orbit coupling and a d_{xy}-wave superconductor without intrinsic spin–orbit coupling, respectively [86]. This result supports our analysis in the main text, where the proximity-induced d_{xy}-wave pair potential in the quasi-one-dimensional thin film is introduced phenomenologically. Proximity effects from high-T_c cuprate superconductors to various two-dimensional materials—such as semiconductor quantum wells [87], graphene [88–90], and MoS_2 [91]—have been demonstrated experimentally. However, whether the induced pairing preserves the original d-wave symmetry remains unclear, as interface roughness often leads to an effective s-wave symmetry instead [92,93]. A detailed assessment of d-wave proximity pairing in the present system would require a more microscopic analysis of a heterostructure combining a high-T_c cuprate superconductor with a PST material, potentially including an intermediate layer to mitigate interface roughness or lattice mismatch. We regard such a microscopic investigation as a crucial future task. In addition, exploring alternative platforms for realizing finite-size topological phases driven by gapped ABSs is an important direction for future work.

In summary, we investigate a novel topological superconducting phase emerging in a Q1D system, where a unidirectional SOC potential of a PST coexists with a d_{xy}-wave pair potential. Finite-size effects lead to hybridization of the flat-band ABSs, resulting in multiple band crossings. Introducing the unidirectional SOC opens a full energy gap in the ABS spectrum and gives rise to an exceptionally large winding number, N_{1D}. Numerical calculations demonstrate the emergence of topologically protected N_{1D}-fold-degenerate ZESs at both ends of the Q1D system. Furthermore, a distinctive perfect transport phenomenon serves as an unambiguous signature of these finite-size-induced topological phases. These findings offer new avenues for studying topological superconducting phases driven by gapped ABSs.

ACKNOWLEDGMENTS

We thank L. Katayama for the fruitful discussion. S.I. is supported by a Grant-in-Aid for Early-Career Scientists (JSPS KAKENHI Grant No. JP24K17010). S.K. was supported by JSPS KAKENHI (Grants No. JP22K03478 and No. JP24K00557) and JST CREST (Grant No. JPMJCR19T2).

DATA AVAILABILITY

The data that support the findings of this article are openly available [94].

APPENDIX A: ZERO-ENERGY BAND CROSSINGS PROTECTED BY INVERSION SYMMETRY

In this Appendix we discuss the relationship between the zero-energy band crossings in Fig. 1(c) and inversion symmetry of the Hamiltonian. In the *absence* of the SOC potential (i.e., $\lambda = 0$), the block component $H_{k_x,s}$ in Eq. (4) preserves inversion symmetry:

$$PH_{k_x,s}P^{-1} = H_{-k_x,s}, \quad P = \begin{bmatrix} P_y & 0 \\ 0 & P_y \end{bmatrix},$$
$$(P_y)_{ij} = \begin{cases} 1 & \text{for } i = M - j + 1 \\ 0 & \text{otherwise} \end{cases}. \tag{A1}$$

This block component also preserves particle-hole-like symmetry:

$$C_P H_{k_x,s} C_P^{-1} = -H_{-k_x,s},$$
$$C_P = \Xi\mathcal{K}, \quad \Xi = \begin{bmatrix} 0 & P_y \\ P_y & 0 \end{bmatrix}, \tag{A2}$$

where the operator C_P satisfies $C_P^2 = +1$. Combining these symmetries, we find CP-like symmetry as

$$U_{CP} H_{k_x,s}^{\mathrm{T}} U_{CP}^{-1} = -H_{k_x,s}, \quad U_{CP} = \Xi P^* = \tau_x, \tag{A3}$$

where $(C_P P)^2 = U_{CP} U_{CP}^* = +1$ and hence $U_{CP}^{\mathrm{T}} = U_{CP}$. Following Refs. [81,82], we define a $\mathbb{Z}_2$ invariant that characterizes the zero-energy band crossings in the spectrum of $H_{k_x,s}$ at $\lambda = 0$. Since U_{CP} is a symmetric matrix, it can be decomposed as $U_{CP} = VQV^{\mathrm{T}}$, where Q is a diagonal matrix and V is a unitary matrix. We define $\Omega = \sqrt{Q}^{\dagger} V^{\dagger}$, where $\sqrt{Q}$ is well defined due to the diagonal nature of Q. Using Ω we rewrite Eq. (A3) as

$$\Omega^* H_{k_x,s}^{\mathrm{T}} \Omega^{\mathrm{T}} = -\Omega H_{k_x,s} \Omega^{\dagger}. \tag{A4}$$

As a result, we find that the transformed Hamiltonian, $\tilde{H}_{k_x,s} = \Omega H_{k_x,s} \Omega^{\dagger}$, becomes an antisymmetric matrix:

$$\tilde{H}_{k_x,s}^{\mathrm{T}} = -\tilde{H}_{k_x,s}. \tag{A5}$$

The antisymmetric nature of $\tilde{H}_{k_x,s}$ allows us to define a $\mathbb{Z}_2$ invariant using its Pfaffian:

$$(-1)^{\nu} = \mathrm{sgn}[\mathrm{Pf}(\tilde{H}_{k',s})\mathrm{Pf}(\tilde{H}_{k'',s})], \tag{A6}$$

where k' and k'' are two arbitrary momenta. When $\nu = 1 \bmod 2$, there is an odd number of zero-energy band crossings between k' and k'' [81,82]. Thus, the presence of zero-energy band crossings in the present system is protected by a nontrivial $\mathbb{Z}_2$ invariant:

$$\mathrm{sgn}\left[\mathrm{Pf}\left(\tilde{H}_{k_n+\delta k,s}\right)\mathrm{Pf}\left(\tilde{H}_{k_n-\delta k,s}\right)\right] = -1, \tag{A7}$$

where k_n denotes the momenta at which zero-energy band crossing occurs and $\delta k \ll 1$. These band crossings can only be removed by perturbations that break the CP-like symmetry in Eq. (A3). In our model such symmetry breaking is achieved by introducing the SOC term (i.e., $\lambda \neq 0$), which inherently breaks the inversion symmetry in Eq. (A1).

APPENDIX B: LOW-ENERGY EFFECTIVE HAMILTONIAN

We derive an effective Hamiltonian in Eq. (13). We begin with the BdG equation in Eq. (7). Using chiral symmetry,

$$\Gamma H_s(k_x,y)\Gamma^{-1} = -H_s(k_x,y), \quad \Gamma = \begin{bmatrix} 0 & -i \\ i & 0 \end{bmatrix}, \tag{B1}$$

we transform the Hamiltonian into the chiral basis for later convenience:

$$\begin{aligned} U_\Gamma H_s(k_x,y)U_\Gamma^\dagger &= Q_s(k_x,y) = Q_s^{d_{xy}}(k_x,y) + Q_s^{\lambda}(y), \\ U_\Gamma &= \frac{1}{\sqrt{2}}\begin{bmatrix} 1 & -i \\ i & -1 \end{bmatrix}, \\ Q_s^{d_{xy}}(k_x,y) &= \begin{bmatrix} 0 & q_s^{d_{xy}}(k_x,y) \\ \{q_s^{d_{xy}}(k_x,y)\}^\dagger & 0 \end{bmatrix}, \\ q_s^{d_{xy}}(k_x,y) &= -i\xi(k_x,y) - \sigma_s\Delta(k_x,y), \\ Q_s^{\lambda}(y) &= \begin{bmatrix} 0 & -i\sigma_s\Lambda(y) \\ i\sigma_s\Lambda(y) & 0 \end{bmatrix}. \end{aligned} \tag{B2}$$

We first examine zero-energy states in the absence of the SOC (i.e., $\lambda = 0$):

$$\begin{aligned} Q_s^{d_{xy}}(k_x,y)\begin{bmatrix} \phi_{s,+}(k_x,y) \\ 0 \end{bmatrix} = 0, \\ Q_s^{d_{xy}}(k_x,y)\begin{bmatrix} 0 \\ \phi_{s,-}(k_x,y) \end{bmatrix} = 0, \end{aligned} \tag{B3}$$

where $\phi_{s,\pm}(k_x,y)$ satisfies

$$\{\pm i\xi(k_x,y) - \sigma_s\Delta(k_x,y)\}\phi_{s,\pm}(k_x,y) = 0. \tag{B4}$$

A general solution takes the form

$$\begin{aligned} \phi_{s,\pm}(k_x,y) &= (ae^{iqy} + be^{-iqy})e^{\pm\sigma_s\tilde{\kappa}y}, \\ q = \sqrt{\tilde{k}_F^2 - \tilde{\kappa}^2}, &\quad \tilde{k}_F = \frac{\sqrt{2m\tilde{\mu}}}{\hbar}, \quad \tilde{\kappa} = \frac{m\tilde{\Delta}}{\hbar^2 k_F}. \end{aligned} \tag{B5}$$

Applying the boundary condition $\phi_{s,\pm}(k_x,0) = 0$, we obtain

$$\phi_{s,\pm}(k_x,y) = c\sin(qy)e^{\pm\sigma_s\tilde{\kappa}y}. \tag{B6}$$

Moreover, the boundary condition, $\phi_{s,\pm}(k_x,W) \propto \sin(qW) = 0$, leads to

$$q = q_n = \frac{n\pi}{W}, \quad n = \pm1, \pm2, \ldots. \tag{B7}$$

From $q = \sqrt{\tilde{k}_F^2 - \tilde{\kappa}^2}$, we find the momenta at which zero-energy states exist:

$$k_x = k_n = \mathrm{sgn}[n]\sqrt{\frac{k_F^2 - q_n^2}{1 + \left(\frac{\Delta}{2\mu}\right)^2}}. \tag{B8}$$

Since k_n must be real, the integer number n is restricted to

$$n = \pm1, \pm2, \ldots, \pm n_c, \tag{B9}$$

where $n_c = [Wk_F/\pi]_G$ represents the number of propagating channels per spin. From the normalization condition,

$$\int_0^W dy\phi_{s,\pm}^*(k_x,y)\phi_{s,\pm}(k_x,y) = 1, \tag{B10}$$

we obtain

$$\begin{aligned} \phi_{s,\pm}(k_n,y) &= c_{k_n,s,\pm}\sin(q_n y)e^{\pm\sigma_s\kappa_n y}, \\ c_{k_n,s,\pm} &= \sqrt{\frac{2X_n}{W}e^{\mp\sigma_s\kappa_n W}}, \\ X_n &= \frac{\kappa_n W}{\sinh(\kappa_n W)}\left\{1 + \left(\frac{\Delta}{2\mu}\right)^2\frac{k_n^2}{q_n^2}\right\}. \end{aligned} \tag{B11}$$

Since $\phi_{s,+}(k_n,y)$ and $\phi_{s,-}(k_n,y)$ are degenerate, we can construct alternative expressions for the zero-energy states by taking linear combinations of these functions. Here, we construct the wave function of the zero-energy states, $\tilde{\psi}_s^\pm(k_n,y) = \sum_{a=\pm} c_{\pm,a}\phi_{s,a}(k_n,y)$, to satisfy

$$\begin{aligned} &\int_0^W dy\{\tilde{\psi}_s^\pm(k_n,y)\}^\dagger Q_s^{d_{xy}}(k_n+\delta k,y)\tilde{\psi}_s^\pm(k_n,y) \\ &\quad = \pm\epsilon_s(k_n+\delta k), \end{aligned} \tag{B12}$$

$$\epsilon_s(k_n+\delta k) = \begin{cases} \mathrm{sgn}[n]|v_n|\delta k + O(\delta k^2) & \text{for } |n| \in \text{odd} \\ -\mathrm{sgn}[n]|v_n|\delta k + O(\delta k^2) & \text{for } |n| \in \text{even} \end{cases}, \tag{B13}$$

where $\pm\epsilon_s(k_x)$ denotes the energy eigenvalues of the ABSs. Equation (B13) means that $\epsilon_s(k_x)$ forms a continuous spectrum with respect to k_x, as illustrated in Fig. 4(a). This is achieved by the wave function

$$\begin{aligned} \tilde{\psi}_s^\pm(k_n,y) &= \begin{cases} e^{\mp i\frac{\pi}{4}}\tilde{\varphi}_s^\pm(k_n,y) & \text{for } |n| \in \text{odd} \\ e^{\mp i\frac{\pi}{4}}\tilde{\varphi}_s^\mp(k_n,y) & \text{for } |n| \in \text{even} \end{cases}, \\ \tilde{\varphi}_s^\pm(k_n,y) &= \frac{1}{\sqrt{2}}\begin{bmatrix} \phi_{s,+}(k_n,y) \\ \pm i\phi_{s,-}(k_n,y) \end{bmatrix}, \end{aligned} \tag{B14}$$

where we specifically obtain

$$v_n = \frac{\hbar^2 k_n}{m}\left\{1 + \left(\frac{\Delta}{2\mu}\right)^2\right\}X_n. \tag{B15}$$

In the main text, we discuss the wave function in the original basis:

$$\psi_s^\pm(k_n,y) = U_\Gamma^\dagger\tilde{\psi}_s^\pm(k_n,y). \tag{B16}$$

To proceed with our analysis, we treat the SOC, $H_s^\lambda(y)$, as a perturbation and construct the low-energy effective Hamiltonian as follows:

$$\begin{aligned} H_s^{\mathrm{eff}}(k_x) &= \begin{bmatrix} A_{++} & A_{+-} \\ A_{-+} & A_{--} \end{bmatrix} + O(\lambda^2), \\ A_{\eta\eta'} &= \int_0^W dy\{\psi_s^\eta(k_x,y)\}^\dagger H_s(k_x,y)\psi_s^{\eta'}(k_x,y), \end{aligned} \tag{B17}$$

where $\psi_s^\pm(k_x,y)$ represents the wave function of the ABSs at $\lambda = 0$, and $A_{\eta\eta} = \eta\epsilon_s(k_x)$. In the vicinity of $k_x = k_n$, we

obtain

$$H_s^{\rm eff}(k_n+\delta k) = \int_0^W dy \begin{bmatrix} \{\tilde{\psi}_s^+(k_n,y)\}^\dagger Q_s(k_n+\delta k,y)\tilde{\psi}_s^+(k_n,y) & \{\tilde{\psi}_s^+(k_n,y)\}^\dagger Q_s(k_n+\delta k,y)\tilde{\psi}_s^-(k_n,y) \\ \{\tilde{\psi}_s^-(k_n,y)\}^\dagger Q_s(k_n+\delta k,y)\tilde{\psi}_s^+(k_n,y) & \{\tilde{\psi}_s^-(k_n,y)\}^\dagger Q_s(k_n+\delta k,y)\tilde{\psi}_s^-(k_n,y) \end{bmatrix} + O(\delta k^2)$$
$$= H_{n,s}^{\rm eff}(\delta k) + O(\delta k^2), \tag{B18}$$

with

$$H_{n,s}^{\rm eff}(\delta k) = \begin{cases} \begin{bmatrix} v_n\delta k & m_n \\ m_n & -v_n\delta k \end{bmatrix} & \text{for } |n| \in \text{odd} \\ \begin{bmatrix} -v_n\delta k & -m_n \\ -m_n & v_n\delta k \end{bmatrix} & \text{for } |n| \in \text{even} \end{cases},$$
$$m_n = \tilde{\lambda}\kappa_n X_n, \tag{B19}$$

which is equivalent to Eq. (13) in the main text.

APPENDIX C: WINDING NUMBER OF THE EFFECTIVE HAMILTONIAN

In this Appendix we compute the one-dimensional winding number of the effective Hamiltonian $H_{n,s}^{\rm eff}(k)$ in Eq. (12). By using an appropriate expression of $\psi_s^\pm(k_x,y)$, we can always construct the effective Hamiltonian preserving chiral symmetry as

$$\gamma H_s^{\rm eff}(k_x)\gamma^{-1} = -H_s^{\rm eff}(k_x), \quad \gamma = \begin{bmatrix} 0 & -i \\ i & 0 \end{bmatrix}, \tag{C1}$$

which allows us to define the winding number,

$$N_{\rm 1D}^{\rm eff} = \frac{i}{4\pi}\sum_{s=\uparrow,\downarrow}\int dk_x {\rm Tr}\left[\gamma\left\{H_s^{\rm eff}(k_x)\right\}^{-1}\partial_{k_x}H_s^{\rm eff}(k_x)\right]. \tag{C2}$$

The effective Hamiltonian can be generally deformed into the chiral basis as

$$U_\gamma H_s^{\rm eff}(k_x)U_\gamma^\dagger = \begin{bmatrix} 0 & q_s(k_x) \\ q_s^*(k_x) & 0 \end{bmatrix},$$
$$U_\gamma = \frac{1}{\sqrt{2}}\begin{bmatrix} 1 & -i \\ i & -1 \end{bmatrix}, \tag{C3}$$

where

$$q_s(k_n+\delta k) = \begin{cases} -iv_n\delta k - m_n & \text{for } |n| \in \text{odd} \\ iv_n\delta k + m_n & \text{for } |n| \in \text{even} \end{cases}. \tag{C4}$$

As shown in Ref. [60], the winding number can be further simplified to

$$N_{\rm 1D}^{\rm eff} = \frac{1}{2}\sum_{s=\uparrow,\downarrow}\sum_{C(k_x)=0}{\rm sgn}[\partial_{k_x}C(k_x)]{\rm sgn}[R(k_x)],$$
$$R(k_x) = {\rm Re}[q_s(k_x)], \quad C(k_x) = {\rm Im}[q_s(k_x)], \tag{C5}$$

where the summation $\sum_{C(k_x)=0}$ is taken for k_x, satisfying $C(k_x)=0$. Using this formula, we eventually obtain

$$N_{\rm 1D}^{\rm eff} = \frac{1}{2}\sum_{s=\uparrow,\downarrow}\sum_{n=-n_c}^{n_c}{\rm sgn}[v_n]{\rm sgn}[m_n] = N_c, \tag{C6}$$

which is also shown in the main text.

APPENDIX D: ZERO-ENERGY STATES IN A BILAYER HAMILTONIAN

In this section we confirm that highly degenerate ZESs can appear in the bilayer Hamiltonian, where the first and second layers describe a nonsuperconducting quasi-one-dimensional thin film with unidirectional SOC and a d_{xy}-wave superconductor without intrinsic SOC, respectively. Specifically, the BdG Hamiltonian on a square lattice reads

$$\begin{aligned} H =& H_{d_{xy}} + H_{\rm psh} + H_t, \\ H_{d_{xy}} =& -t_s\sum_{\boldsymbol{r}\in S}\sum_{\sigma=\uparrow,\downarrow}\sum_{\boldsymbol{v}=\boldsymbol{x},\boldsymbol{y}}(c_{\boldsymbol{r}+\boldsymbol{v},\sigma}^\dagger c_{\boldsymbol{r},\sigma} + {\rm H.c.}) + (4t_s-\mu_s)\sum_{\boldsymbol{r},\sigma}c_{\boldsymbol{r},\sigma}^\dagger c_{\boldsymbol{r},\sigma} \\ &+ \frac{\Delta}{4}\sum_{\boldsymbol{r}\in S}\left\{(c_{\boldsymbol{r}+\boldsymbol{x}+\boldsymbol{y},\uparrow}^\dagger c_{\boldsymbol{r},\downarrow}^\dagger + c_{\boldsymbol{r},\uparrow}^\dagger c_{\boldsymbol{r}+\boldsymbol{x}+\boldsymbol{y},\downarrow}^\dagger - c_{\boldsymbol{r}+\boldsymbol{x}-\boldsymbol{y},\uparrow}^\dagger c_{\boldsymbol{r},\downarrow}^\dagger - c_{\boldsymbol{r},\uparrow}^\dagger c_{\boldsymbol{r}+\boldsymbol{x}-\boldsymbol{y},\downarrow}^\dagger) + {\rm H.c.}\right\}, \\ H_{\rm psh} =& -t_n\sum_{\boldsymbol{r}\in N}\sum_{\sigma}\sum_{\boldsymbol{v}=\boldsymbol{x},\boldsymbol{y}}(d_{\boldsymbol{r}+\boldsymbol{v},\sigma}^\dagger d_{\boldsymbol{r},\sigma} + {\rm H.c.}) + (4t_n-\mu_n)\sum_{\boldsymbol{r},\sigma}d_{\boldsymbol{r},\sigma}^\dagger d_{\boldsymbol{r},\sigma} \\ &+ \frac{i\lambda}{2}\sum_{\boldsymbol{r}\in N}\sum_{\sigma}s_\sigma(d_{\boldsymbol{r}+\boldsymbol{y},\sigma}^\dagger d_{\boldsymbol{r},\sigma} - d_{\boldsymbol{r},\sigma}^\dagger d_{\boldsymbol{r}+\boldsymbol{y},\sigma}) \\ H_t =& -t'\sum_{\boldsymbol{r}\in N}\sum_{\sigma}(d_{\boldsymbol{r},\sigma}^\dagger c_{\boldsymbol{r},\sigma} + {\rm H.c.}), \end{aligned} \tag{D1}$$

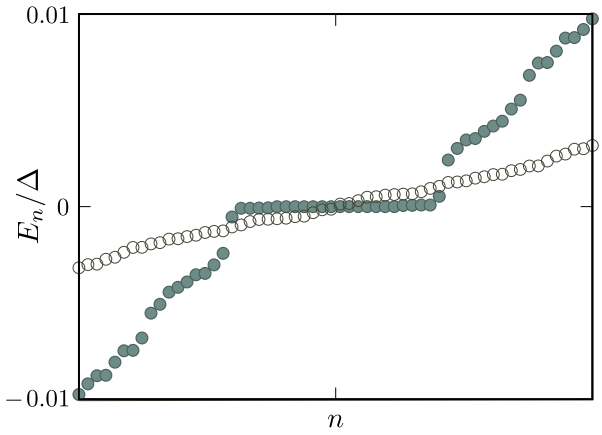

FIG. 6. Energy spectrum of the full Hamiltonian, where the colored (white) dots indicate the result for $\lambda = 0.5t$ ($\lambda = 0$). Each dot corresponds to twofold-degenerate states due to Kramars degeneracy. For $\lambda = 0.5t$, we clearly observe the emergence of highly degenerate zero-energy states.

where $c_{\boldsymbol{r},\sigma}$ ($d_{\boldsymbol{r},\sigma}$) is the annihilation operator of an electron at a site $\boldsymbol{r}$ with spin σ in the d_{xy}-wave superconductor (quasi-one-dimensional wire), and $\sum_{\boldsymbol{r}\in S}$ ($\sum_{\boldsymbol{r}\in N}$) represents the summation over the lattice sites in the superconducting layer (quasi-one-dimensional wire). The coupling between the d_{xy}-wave superconductor and quasi-one-dimensional wire is described by H_t. The d_{xy}-wave superconductor has length 3000 and width 530 in units of lattice spacing. For the d_{xy}-wave superconductor, we apply periodic boundary conditions in both x and y direction to eliminate the flat-band ABSs in the superconducting layer. The quasi-one-dimensional wire has length 2500 and width 30, with open boundary conditions applied in both x and y direction. We obtain the low-energy eigenvalues using the Sakurai–Sugiura method [86]. In Fig. 6 we show the energy eigenvalues for $t_s = t_n = t'$, $\mu_s = \mu_n = 2t_s$, and $\Delta = 0.2t_s$. The colored (white) dots indicate the result for $\lambda = 0.5t$ ($\lambda = 0$); each dot represents a twofold-degenerate state caused by Kramers degeneracy. Since the d_{xy}-wave superconductor layer is nodal, the energy spectrum of the bilayer Hamiltonian does not exhibit a substantial energy gap. Nevertheless, we find that highly degenerate zero-energy states appear only in the presence of SOC potential, supporting the results in the main text, where the proximity-induced d_{xy}-wave pair potential in the quasi-one-dimensional wire is introduced phenomenologically.

[1] C. Nayak, S. H. Simon, A. Stern, M. Freedman, and S. Das Sarma, Non-Abelian anyons and topological quantum computation, Rev. Mod. Phys. **80**, 1083 (2008).

[2] M. Z. Hasan and C. L. Kane, Colloquium: Topological insulators, Rev. Mod. Phys. **82**, 3045 (2010).

[3] X.-L. Qi and S.-C. Zhang, Topological insulators and superconductors, Rev. Mod. Phys. **83**, 1057 (2011).

[4] A. Bansil, H. Lin, and T. Das, Colloquium: Topological band theory, Rev. Mod. Phys. **88**, 021004 (2016).

[5] M. Sato and Y. Ando, Topological superconductors: A review, Rep. Prog. Phys. **80**, 076501 (2017).

[6] A. P. Schnyder, S. Ryu, A. Furusaki, and A. W. W. Ludwig, Classification of topological insulators and superconductors in three spatial dimensions, Phys. Rev. B **78**, 195125 (2008).

[7] Y. Zhang, K. He, C.-Z. Chang, C.-L. Song, L.-L. Wang, X. Chen, J.-F. Jia, Z. Fang, X. Dai, W.-Y. Shan, S.-Q. Shen, Q. Niu, X.-L. Qi, S.-C. Zhang, X.-C. Ma, and Q.-K. Xue, Crossover of the three-dimensional topological insulator Bi_2Se_2 to the two-dimensional limit, Nat. Phys. **6**, 584 (2010).

[8] A. C. Potter and P. A. Lee, Multichannel generalization of Kitaev's Majorana end states and a practical route to realize them in thin films, Phys. Rev. Lett. **105**, 227003 (2010).

[9] Y. Sakamoto, T. Hirahara, H. Miyazaki, S.-I. Kimura, and S. Hasegawa, Spectroscopic evidence of a topological quantum phase transition in ultrathin Bi_2Se_3 films, Phys. Rev. B **81**, 165432 (2010).

[10] A. A. Taskin, S. Sasaki, K. Segawa, and Y. Ando, Manifestation of topological protection in transport properties of epitaxial Bi_2Se_3 thin films, Phys. Rev. Lett. **109**, 066803 (2012).

[11] S. K. Chong, L. Liu, K. Watanabe, T. Taniguchi, T. D. Sparks, F. Liu, and V. V. Deshpande, Emergent helical edge states in a hybridized three-dimensional topological insulator, Nat. Commun. **13**, 6386 (2022).

[12] J. Linder, T. Yokoyama, and A. Sudbø, Anomalous finite size effects on surface states in the topological insulator Bi_2Se_3, Phys. Rev. B **80**, 205401 (2009).

[13] C.-X. Liu, H. Zhang, B. Yan, X.-L. Qi, T. Frauenheim, X. Dai, Z. Fang, and S.-C. Zhang, Oscillatory crossover from two-dimensional to three-dimensional topological insulators, Phys. Rev. B **81**, 041307(R) (2010).

[14] R. Yu, W. Zhang, H.-J. Zhang, S.-C. Zhang, X. Dai, and Z. Fang, Quantized anomalous Hall effect in magnetic topological insulators, Science **329**, 61 (2010).

[15] F. Zhang, C. L. Kane, and E. J. Mele, Time-reversal-invariant topological superconductivity and Majorana Kramers pairs, Phys. Rev. Lett. **111**, 056402 (2013).

[16] R.-X. Zhang and S. Das Sarma, Intrinsic time-reversal-invariant topological superconductivity in thin films of iron-based superconductors, Phys. Rev. Lett. **126**, 137001 (2021).

[17] L. Fu and C. L. Kane, Superconducting proximity effect and Majorana fermions at the surface of a topological insulator, Phys. Rev. Lett. **100**, 096407 (2008).

[18] H.-Z. Lu, W.-Y. Shan, W. Yao, Q. Niu, and S.-Q. Shen, Massive Dirac fermions and spin physics in an ultrathin film of topological insulator, Phys. Rev. B **81**, 115407 (2010).

[19] W.-Y. Shan, H.-Z. Lu, and S.-Q. Shen, Effective continuous model for surface states and thin films of three-dimensional topological insulators, New J. Phys. **12**, 043048 (2010).

[20] K. Ebihara, K. Yada, A. Yamakage, and Y. Tanaka, Finite size effects of the surface states in a lattice model of topological insulator, Physica E **44**, 885 (2012).

[21] H. Ozawa, A. Yamakage, M. Sato, and Y. Tanaka, Topological phase transition in a topological crystalline insulator induced by finite-size effects, Phys. Rev. B **90**, 045309 (2014).

[22] B.-J. Yang and N. Nagaosa, Emergent topological phenomena in thin films of pyrochlore iridates, Phys. Rev. Lett. **112**, 246402 (2014).

[23] J. Wang, Q. Zhou, B. Lian, and S.-C. Zhang, Chiral topological superconductor and half-integer conductance plateau from quantum anomalous Hall plateau transition, Phys. Rev. B **92**, 064520 (2015).

[24] M. M. Asmar, D. E. Sheehy, and I. Vekhter, Topological phases of topological-insulator thin films, Phys. Rev. B **97**, 075419 (2018).

[25] X. Wu, W. A. Benalcazar, Y. Li, R. Thomale, C.-X. Liu, and J. Hu, Boundary-obstructed topological high-T_c superconductivity in iron pnictides, Phys. Rev. X **10**, 041014 (2020).

[26] A. M. Cook and Anne E. B. Nielsen, Finite-size topology, Phys. Rev. B **108**, 045144 (2023).

[27] R. Flores-Calderon, R. Moessner, and A. M. Cook, Time-reversal invariant finite-size topology, Phys. Rev. B **108**, 125410 (2023).

[28] A. Pal and A. M. Cook, Finite-size topological phases from semimetals, Phys. Rev. B **111**, 035146 (2025).

[29] P. Hosur, P. Ghaemi, R. S. K. Mong, and A. Vishwanath, Majorana modes at the ends of superconductor vortices in doped topological insulators, Phys. Rev. Lett. **107**, 097001 (2011).

[30] C. Fang, M. J. Gilbert, and B. A. Bernevig, New class of topological superconductors protected by magnetic group symmetries, Phys. Rev. Lett. **112**, 106401 (2014).

[31] G. Xu, B. Lian, P. Tang, X.-L. Qi, and S.-C. Zhang, Topological superconductivity on the surface of Fe-based superconductors, Phys. Rev. Lett. **117**, 047001 (2016).

[32] S. Qin, L. Hu, C. Le, J. Zeng, F. C. Zhang, C. Fang, and J. Hu, Quasi-1D topological nodal vortex line phase in doped superconducting 3D Dirac semimetals, Phys. Rev. Lett. **123**, 027003 (2019).

[33] E. J. König and P. Coleman, Crystalline-symmetry-protected helical Majorana modes in the iron pnictides, Phys. Rev. Lett. **122**, 207001 (2019).

[34] S. Kobayashi and A. Furusaki, Double Majorana vortex zero modes in superconducting topological crystalline insulators with surface rotation anomaly, Phys. Rev. B **102**, 180505(R) (2020).

[35] Z. Yan, Z. Wu, and W. Huang, Vortex end Majorana zero modes in superconducting Dirac and Weyl semimetals, Phys. Rev. Lett. **124**, 257001 (2020).

[36] R. Giwa and P. Hosur, Fermi arc criterion for surface Majorana modes in superconducting time-reversal symmetric Weyl semimetals, Phys. Rev. Lett. **127**, 187002 (2021).

[37] L.-H. Hu, X. Wu, C.-X. Liu, and R.-X. Zhang, Competing vortex topologies in iron-based superconductors, Phys. Rev. Lett. **129**, 277001 (2022).

[38] S. Kobayashi, S. Sumita, M. Hirayama, and A. Furusaki, Crystal symmetry protected gapless vortex line phases in superconducting Dirac semimetals, Phys. Rev. B **107**, 214518 (2023).

[39] L.-H. Hu and R.-X. Zhang, Topological superconducting vortex from trivial electronic bands, Nat. Commun. **14**, 640 (2023).

[40] B. Zhou and S.-Q. Shen, Crossover from Majorana edge- to end-states in quasi-one-dimensional p-wave superconductors, Phys. Rev. B **84**, 054532 (2011).

[41] C.-Z. Chen, Y.-M. Xie, J. Liu, P. A. Lee, and K. T. Law, Quasi-one-dimensional quantum anomalous Hall systems as new platforms for scalable topological quantum computation, Phys. Rev. B **97**, 104504 (2018).

[42] B. A. Bernevig, J. Orenstein, and S.-C. Zhang, Exact SU(2) symmetry and persistent spin Helix in a spin-orbit coupled system, Phys. Rev. Lett. **97**, 236601 (2006).

[43] J. Schliemann, Colloquium: Persistent spin textures in semiconductor nanostructures, Rev. Mod. Phys. **89**, 011001 (2017).

[44] M. Kohda and G. Salis, Physics and application of persistent spin Helix state in semiconductor heterostructures, Semicond. Sci. Technol. **32**, 073002 (2017).

[45] M. A. U. Absor, F. Ishii, H. Kotaka, and M. Saito, Persistent spin Helix on a wurtzite ZnO $(10\bar{1}0)$ surface: First-principles density-functional study, Appl. Phys. Express **8**, 073006 (2015).

[46] L. L. Tao and E. Y. Tsymbal, Persistent spin texture enforced by symmetry, Nat. Commun. **9**, 2763 (2018).

[47] H. Djani, A. C. Garcia-Castro, W.-Y. Tong, P. Barone, E. Bousquet, S. Picozzi, and P. Ghosez, Rationalizing and engineering Rashba spin-splitting in ferroelectric oxides, npj Quantum Mater. **4**, 51 (2019).

[48] C. Autieri, P. Barone, J. Sławińska, and S. Picozzi, Persistent spin Helix in Rashba-Dresselhaus ferroelectric $CsBiNb_2O_7$, Phys. Rev. Mater. **3**, 084416 (2019).

[49] H. Lee, J. Im, and H. Jin, Emergence of the giant out-of-plane Rashba effect and tunable nanoscale persistent spin Helix in ferroelectric SnTe thin films, Appl. Phys. Lett. **116**, 022411 (2020).

[50] F. Jia, S. Hu, S. Xu, H. Gao, G. Zhao, P. Barone, Al Stroppa, and W. Ren, Persistent spin-texture and ferroelectric polarization in 2D hybrid perovskite benzylammonium lead-halide, J. Phys. Chem. Lett. **11**, 5177 (2020).

[51] X.-Z. Lu and J. M. Rondinelli, Discovery principles and materials for symmetry-protected persistent spin textures with long spin lifetimes, Matter **3**, 1211 (2020).

[52] N. Yang, G. Gou, X. Lu, and Y. Hao, Linear dichroism and polarization controllable persistent spin Helix in two-dimensional ferroelectric $ZrOI_2$ monolayer, Nano Res. **15**, 6779 (2022).

[53] X. Li, S. Zhang, H. Huang, L. Hu, F. Liu, and Q. Wang, Unidirectional spin-orbit interaction induced by the line defect in monolayer transition metal dichalcogenides for high-performance devices, Nano Lett. **19**, 6005 (2019).

[54] M. A. U. Absor, I. Santoso, N. Yamaguchi, and F. Ishii, Spin splitting with persistent spin textures induced by the line defect in the $1T$ phase of monolayer transition metal dichalcogenides, Phys. Rev. B **101**, 155410 (2020).

[55] M. A. U. Absor, A. Lukmantoro, and I. Santoso, Full-zone persistent spin textures with giant spin splitting in two-dimensional group IV–V compounds, J. Phys.: Condens. Matter **34**, 445501 (2022).

[56] C. Bruder, Andreev scattering in anisotropic superconductors, Phys. Rev. B **41**, 4017 (1990).

[57] C.-R. Hu, Midgap surface states as a novel signature for $d_{x_a^2-x_b^2}$-wave superconductivity, Phys. Rev. Lett. **72**, 1526 (1994).

[58] Y. Tanaka and S. Kashiwaya, Theory of tunneling spectroscopy of d-wave superconductors, Phys. Rev. Lett. **74**, 3451 (1995).

[59] Y. Asano, Y. Tanaka, and S. Kashiwaya, Phenomenological theory of zero-energy Andreev resonant states, Phys. Rev. B **69**, 134501 (2004).

[60] M. Sato, Y. Tanaka, K. Yada, and T. Yokoyama, Topology of Andreev bound states with flat dispersion, Phys. Rev. B **83**, 224511 (2011).

[61] Y. Tanaka and S. Kashiwaya, Anomalous charge transport in triplet superconductor junctions, Phys. Rev. B **70**, 012507 (2004).

[62] Y. Tanaka, S. Kashiwaya, and T. Yokoyama, Theory of enhanced proximity effect by midgap Andreev resonant state in diffusive normal-metal/triplet superconductor junctions, Phys. Rev. B **71**, 094513 (2005).

[63] Y. Asano, Y. Tanaka, A. A. Golubov, and S. Kashiwaya, Conductance spectroscopy of spin-triplet superconductors, Phys. Rev. Lett. **99**, 067005 (2007).

[64] S. Ikegaya, Y. Asano, and Y. Tanaka, Anomalous proximity effect and theoretical design for its realization, Phys. Rev. B **91**, 174511 (2015).

[65] S. Ikegaya, S.-I. Suzuki, Y. Tanaka, and Y. Asano, Quantization of conductance minimum and index theorem, Phys. Rev. B **94**, 054512 (2016).

[66] S. Ikegaya, J. Lee, A. P. Schnyder, and Y. Asano, Strong anomalous proximity effect from spin-singlet superconductors, Phys. Rev. B **104**, L020502 (2021).

[67] J. Lee, S. Ikegaya, and Y. Asano, Anomalous proximity effect of a spin-singlet superconductor with a spin-orbit interaction, Phys. Rev. B **111**, 174516 (2025).

[68] Y. Nagae, L. Katayama, and S. Ikegaya, Majorana flat bands and anomalous proximity effects in p-wave magnet–superconductor hybrid systems, Phys. Rev. B **111**, 174519 (2025).

[69] Y. Asano, Y. Tanaka, and S. Kashiwaya, Anomalous Josephson effect in p-wave dirty junctions, Phys. Rev. Lett. **96**, 097007 (2006).

[70] Y. Asano, Y. Tanaka, T. Yokoyama, and S. Kashiwaya, Josephson current through superconductor/diffusive-normal-metal/superconductor junctions: Interference effects governed by pairing symmetry, Phys. Rev. B **74**, 064507 (2006).

[71] S. Ikegaya and Y. Asano, Degeneracy of Majorana bound states and fractional Josephson effect in a dirty SNS junction, J. Phys.: Condens. Matter **28**, 375702 (2016).

[72] A. Damascelli, Z. Hussain, and Z.-X. Shen, Angle-resolved photoemission studies of the cuprate superconductors, Rev. Mod. Phys. **75**, 473 (2003).

[73] M. Hashimoto, I. M. Vishik, R.-H. He, T. P. Devereaux, and Z.-X. Shen, Energy gaps in high-transition-temperature cuprate superconductors, Nat. Phys. **10**, 483 (2014).

[74] J. Linder and A. Sudbø, Dirac fermions and conductance oscillations in s- and d-wave superconductor-graphene junctions, Phys. Rev. Lett. **99**, 147001 (2007).

[75] J. Linder, A. M. Black-Schaffer, T. Yokoyama, S. Doniach, and A. Sudbø, Josephson current in graphene: Role of unconventional pairing symmetries, Phys. Rev. B **80**, 094522 (2009).

[76] C. L. M. Wong and K. T. Law, Majorana Kramers doublets in $d_{x^2-y^2}$-wave superconductors with Rashba spin-orbit coupling, Phys. Rev. B **86**, 184516 (2012).

[77] P. Lucignano, A. Mezzacapo, F. Tafuri, and A. Tagliacozzo, Advantages of using high-temperature cuprate superconductor heterostructures in the search for Majorana fermions, Phys. Rev. B **86**, 144513 (2012).

[78] J. Linder, Y. Tanaka, T. Yokoyama, A. Sudbø, and N. Nagaosa, Unconventional superconductivity on a topological insulator, Phys. Rev. Lett. **104**, 067001 (2010).

[79] Z. Yan, F. Song, and Z. Wang, Majorana corner modes in a high-temperature platform, Phys. Rev. Lett. **121**, 096803 (2018).

[80] T. Liu, J. J. He, and F. Nori, Majorana corner states in a two-dimensional magnetic topological insulator on a high-temperature superconductor, Phys. Rev. B **98**, 245413 (2018).

[81] S. Kobayashi, K. Shiozaki, Y. Tanaka, and M. Sato, Topological Blount's theorem of odd-parity superconductors, Phys. Rev. B **90**, 024516 (2014).

[82] D. F. Agterberg, P. M. R. Brydon, and C. Timm, Bogoliubov Fermi surfaces in superconductors with broken time-reversal symmetry, Phys. Rev. Lett. **118**, 127001 (2017).

[83] G. E. Blonder, M. Tinkham, and T. M. Klapwijk, Transition from metallic to tunneling regimes in superconducting microconstrictions: Excess current, charge imbalance, and supercurrent conversion, Phys. Rev. B **25**, 4515 (1982).

[84] P. A. Lee and D. S. Fisher, Anderson localization in two dimensions, Phys. Rev. Lett. **47**, 882 (1981).

[85] T. Ando, Quantum point contacts in magnetic fields, Phys. Rev. B **44**, 8017 (1991).

[86] Y. Nagai, Y. Shinohara, Y. Futamura, Y. Ota, and T. Sakurai, Numerical construction of a low-energy effective Hamiltonian in a self-consistent Bogoliubov–de Gennes approach of superconductivity, J. Phys. Soc. Jpn. **82**, 094701 (2013).

[87] A. Hayat, P. Zareapour, S. Y. F. Zhao, A. Jain, I. G. Savelyev, M. Blumin, Z. Xu, A. Yang, G. D. Gu, H. E. Ruda, S. Jia, R. J. Cava, A. M. Steinberg, and K. S. Burch, Hybrid high-temperature-superconductor—semiconductor tunnel diode, Phys. Rev. X **2**, 041019 (2012).

[88] A. D. Bernardo, O. Millo, M. Barbone, H. Alpern, Y. Kalcheim, U. Sassi, A. K. Ott, D. D. Fazio, D. Yoon, M. Amado, A. C. Ferrari, J. Linder, and J. W. A. Robinson, p-wave triggered superconductivity in single-layer graphene on an electron-doped oxide superconductor, Nat. Commun. **8**, 14024 (2017).

[89] D. Perconte, F. A. Cuellar, C. Moreau-Luchaire, M. Piquemal-Banci, R. Galceran, P. R. Kidambi, M.-B. Martin, S. Hofmann, R. Bernard, B. Dlubak, P. Seneor, and J. E. Villegas, Tunable Klein-like tunneling of high-temperature superconducting pairs into graphene, Nat. Phys. **14**, 25 (2018).

[90] D. Perconte, K. Seurre, V. Humbert, C. Ulysse, A. Sander, J. Trastoy, V. Zatko, F. Godel, P. R. Kidambi, S. Hofmann, X. P. Zhang, D. Bercioux, F. S. Bergeret, B. Dlubak, P. Seneor, and J. E. Villegas, Long-range propagation and interference of d-wave superconducting pairs in graphene, Phys. Rev. Lett. **125**, 087002 (2020).

[91] K. Seurre, M. Ayachi, F. Godel, S. J. Carreira, B. Dlubak, P. Seneor, V. Humbert, and J. E. Villegas, Large-scale integration of MoS_2 on high-T_C superconducting $YBa_2Cu_3O_7$ for the realization of Josephson devices, Appl. Phys. Lett. **125**, 092603 (2024).

[92] A. A. Golubov and M. Yu Kupriyanov, Anomalous proximity effect in d-wave superconductors, J. Exp. Theor. Phys. Lett. **67**, 501 (1998).

[93] Z.-X. Li, C. Chan, and H. Yao, Realizing Majorana zero modes by proximity effect between topological insulators and d-wave high-temperature superconductors, Phys. Rev. B **91**, 235143 (2015).

[94] https://github.com/ikegayas/data_2504.06524.